

# The Molecular Aharonov-Bohm Effect Redux\*

B. Zygelman

*Department of Physics and Astronomy, University of Nevada, Las Vegas, USA*

A solvable molecular collision model that predicts Aharonov-Bohm (AB) like scattering in the adiabatic approximation is introduced. For it, we propagate coupled channel wave packets without resorting to a Born-Oppenheimer (BO) approximation. In those, exact, solutions we find evidence of topological phase dislocation lines that are independent of the collision energy and provide definitive signatures of AB-like scattering. The results of these simulations contrast with the conclusions of a recent study that suggests survival of the molecular Aharonov-Bohm (MAB) effect only in the adiabatic limit in which the nuclear reduced mass  $\mu \rightarrow \infty$ . We discuss generalizations of this model and consider possible screening of the Mead-Truhlar vector potential by the presence of multiple conical intersections (CI). We demonstrate that the Wilson loop phase integral has the value  $-1$  if it encloses an odd-number of CI's, and takes the value  $+1$  for an even number. Within the scope of this model, we investigate the ultra-cold limit of scattering solutions in the presence of a conical intersection and comment on the relevance of Wigner threshold behavior for s-wave scattering.

## I. INTRODUCTION

The Aharonov-Bohm effect[1, 2] describes the behavior of a charged particle in the presence of a gauge vector potential that does not impress a Lorentz force on the particle, but nevertheless exerts a profound influence on its scattering properties. Importantly, it is a topological effect and, as such, has served as a template in understanding the behavior of exotic forms of quantum matter including anyons[3], quantum Hall systems[4], and topological insulators[5].

In molecular physics, an analog of the AB effect was discovered by Mead and Truhlar[6] in their analysis of polyatomic systems whose electronic Born-Oppenheimer surfaces possess a conical intersection. They showed how, in the ground BO surface that shares a CI with an excited electronic BO state, the motion of atoms are minimally coupled to an effective vector potential similar to that which describes a magnetic flux tube

$$\mathbf{A} = \hat{\phi} \frac{\Phi}{2\pi R}. \quad (1)$$

Here  $\Phi$  is the magnetic flux enclosed by the (infinitesimal) tube running along the z-axis in a cylindrical coordinate system in which  $\hat{\phi}$  is the azimuthal unit vector and  $R$  is the distance from the flux tube. The scattering amplitude is proportional to the enclosed magnetic flux provided that  $\Phi/2\pi \neq n$ , where  $n$  is an integer. In the Mead-Truhlar analysis the molecular reaction coordinates are coupled to this vector potential for the case  $\Phi = \pi$  which we henceforth label as  $\mathbf{A}_{MAB}$ . It arises due to the properties of the BO electronic wavefunctions near a CI and which is the locus of an effective flux tube. According to AB theory,  $\mathbf{A}_{MAB}$  should give rise to topological effects in a reactive scattering setting and has therefore been called the molecular Aharonov-Bohm effect (MAB).

The bound state Aharonov-Bohm effect[7, 8] describes the shift in the eigenenergies of a bound system in the vicinity of such a flux tube. It is in this context that the MAB effect was first observed in a laboratory setting [9, 10]. In Jahn-Teller (JT)[9, 11] systems, in which the atoms are subjected to a bounding “Mexican hat” scalar potential circumscribing the conical intersection vibrational eigenvalues are shifted, and have been detected in spectroscopic studies

Despite the success of the gauge paradigm to predict bound state energy shifts in Jahn-Teller systems, more than a quarter century of effort in both theoretical and experimental arenas have failed to provide a clear signature for the molecular AB effect in a reactive scattering scenario. Early theoretical studies[12] of the rovibrational product distribution in reactive scattering of the  $H + H_2$  system, included the MAB effect and promised to resolve[13] existing discrepancies between experiment[14] and theory. Subsequently, additional theoretical efforts and experiments showed that the issue is not so clear cut[15–19]. For example, more recent experimental measurements[15] for product state distributions are in excellent agreement with calculations that omit the MAB effect[17].

Theoretical and numerical studies of the MAB effect in reactive scattering systems fall into two categories. In the first, an adiabatic approximation is employed and non-adiabatic couplings to states other than the ground electronic states are ignored. The ground state amplitude is minimally coupled to  $\mathbf{A}_{MAB}$ , or boundary conditions on the vibronic amplitude are imposed so that the product of vibronic and the ground (multi-valued) electronic amplitudes is single-valued. In the second category, a two-state approximation which includes both the ground and excited electronic states that share a CI are incorporated. That approach leads to a pair of coupled Schrodinger-like equations, and it has been argued that, in this case, it is not necessary to include  $\mathbf{A}_{MAB}$ . In a recent numerical study[20] adiabaticity was relaxed in a so-called exact treatment of a model system that possesses a CI. In those calculations it was found that the MAB effect sur-

\* bernard@physics.unlv.edu

vives only in the limit in which the effective mass for the vibronic motion tends to infinity. That result suggests that evidence of a MAB effect, cited in studies based on the BO approximation, may be an artifact of the latter. In calculations involving realistic systems, issues such as the accuracy of potential surfaces, inclusion of rotational and other couplings, accommodation of realistic asymptotic boundary conditions, arise and need to be addressed in a rigorous and un-ambiguous manner. For example, it is known[21, 22] that rotational couplings can also be described by an effective vector gauge potential. The latter may lead to phase holonomies that interfere with those generated by  $\mathbf{A}_{MAB}$ .

Because of the cited discrepancy and the lack of a clear experimental signature, we are motivated to re-consider the question; is the MAB effect an artifact of an adiabatic approximation? Definitive predictions and validation requires a system that exhibits the requisite complexity, i.e. it possesses a CI, but at the same time it must be simple enough to allow accurate numerical solution. In the discussion below, we introduce such a model and offer exact numerical solutions that are not limited by adiabatic assumptions. Though it does not describe a realistic molecular system, it shares essential features of the latter and predictions gleaned from it enhance our understanding of MAB phenomena in general. Before introducing and solving the proposed model, we first review classical pure AB scattering[1], and sharpen our understanding of what it means for the latter to be a topological effect.

### A. Classical AB scattering

Consider an incoming packet with de-Broglie wavelength  $\lambda$  impinging on the magnetic flux tube described by vector potential Eq.(1). The particle is scattered by it and, in a time independent description, the differential scattering cross section (per unit length) is[1],

$$\lambda \frac{d\sigma}{d\theta} = \frac{\sin^2 \pi\alpha}{\cos^2 \theta/2} \quad (2)$$

where  $\alpha \equiv e\Phi/h$ , and  $\theta$  is the angle measured from the incident (+x direction) flux. The right hand side of Eq. (2) is independent of the collision energy and is a reflection of the topological nature of AB scattering. Consider now the case where the flux tube is embedded along the axis of an impenetrable cylinder of radius  $a$ . We then have a scenario in which the scattering amplitude of the short range potential (of the cylinder) interferes with that of the long-range nature of Eq. (1). The total wave functions is now described by[23]

$$\begin{aligned} \psi(r, \theta) &= \psi_{AB}(r, \theta) - \psi_a(r, \theta) \\ \psi_a(r, \theta) &= \sum_m (-i)^{|m-\alpha|} \exp(im\theta) \frac{J_{|m-\alpha|}(ka)}{H_{|m-\alpha|}^{(1)}(ka)} H_{|m-\alpha|}^{(1)}(kr) \end{aligned} \quad (3)$$

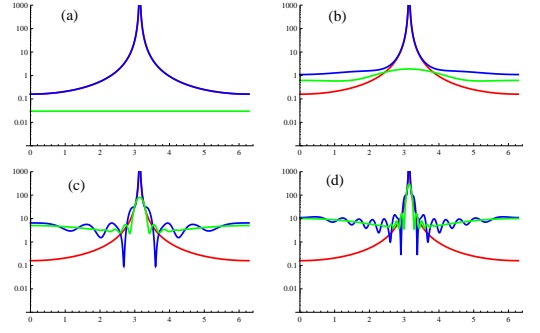


FIG. 1: Plot of  $k d\sigma/d\theta$ , where the abscissa is the scattering angle  $0 \leq \theta < 2\pi$ . Green lines correspond to scattering by the cylinder only, red lines identify pure AB scattering, blue lines denotes scattering by the cylinder including  $\mathbf{A}_{MAB}$ . The panels (a)-(d) correspond to wave numbers  $k = 0.01, 0.1, 1, 10$  respectively.

where  $\psi_{AB}$  is the AB wavefunction and the sum extends over all negative and positive integers  $m$ . For the case  $\alpha = 1/2$ , which corresponds to the MAB value for  $\Phi$ ,  $\psi_{AB}$  has the analytic form[1, 23]

$$\begin{aligned} \psi_{AB} &= -\exp(i\phi/2) \exp(-ik\rho \cos \phi) \times \\ &\quad \text{Erf}(\exp(i3\pi/4)\sqrt{2k\rho} \cos(\phi/2)) \end{aligned} \quad (4)$$

where  $\tan \phi = x/y$ ,  $k^2/2$  is the collision energy and  $0 \leq |\phi| \leq \pi$ . At large  $r = \sqrt{x^2 + y^2}$  it describes an incident wave, approaching from the positive  $x$  direction,

$$\psi_{inc} = \exp(-ikx) \exp(i\phi/2). \quad (5)$$

Though the incident wave appears to be multi-valued, the total amplitude is single-valued[23].

In Figure (1) we plot the differential cross sections, as a function of the scattering angle  $\theta$ , for various values of incoming wavenumbers  $k$  for the cases (i) scattering by an impenetrable cylinder without the presence of a flux tube, (ii) pure AB scattering (no short range potential), (iii) the case described by the wave function Eq. (3). The green lines in panels (a)-(d) give  $k d\sigma/d\theta$  for case (i). At very low collision energies, corresponding to the s-wave scattering limit,  $d\sigma/d\theta$  tends to a constant for all values of  $\theta$ . At higher energies the cross sections exhibit pronounced structures and approaches, at larger  $\theta$ , the classical value (shown by the dotted black line in panel (d)). The strong forward scattering peak is indicative of wave interference (i.e. the 1D analog of the Poisson spot[24]). The red lines are plots of Eq. (2) and are independent of the wave number  $k$ . In panel (a), corresponding to  $k = 0.01$ , the red line is not visible as the blue line overlaps it and represents scattering by an AB flux tube enclosed by an impenetrable cylinder of radius  $a = 1$ . The panels illustrate the interference between the short range interaction with the cylinder and the long range coupling with gauge field  $\mathbf{A}_{MAB}$  for various collision energies. As  $k$  increases we find that interference effects begin to wash out (except for a small region toward the

forward scattering angle) contributions that arise from  $\mathbf{A}_{MAB}$ . In panel (d) the cross sections, given by the blue line, approach that of scattering by the short range interaction only (i.e. the green line).

Though the influence of  $\mathbf{A}_{MAB}$  in Fig. (1) is evident, especially at lower collisions energies, interference with the scattered waves of the short range potential does not offer a compelling demonstration of the inherent topological nature of the former as the collision energy is varied. Inspection of  $d\sigma/d\theta$  (for  $\theta \neq 0$ ) is not an ideal indicator of hidden topological order. Instead, we follow the strategy of Ref. [23] and study features that are topological invariants. In Fig (2) we plot the imaginary part of the total wave function  $\psi(R, \theta)$ , given in Eq. (3). It is the wave function that describes scattering by a short range potential that includes the AB vector potential. In that figure the abscissa represents the  $x$  axis, with the incident wave being scattered by the cylinder, shown as the white circle, at the origin. The horizontal axis defines the  $y$  axis. The leftmost panel corresponds to the wavenumber  $k = 0.01$ , the middle panel to  $k = 1$ , and the rightmost panel to  $k = 10$ . In those figures we find, as expected, complex interference structures between incident and scattered waves as the collision energy is varied. However, we also note prominent a phase dislocation line (which corresponds to a nodal line of the total amplitude) that originate at the origin and extends along the negative  $x$  axis. These features, unlike  $d\sigma/d\omega$ , remain fixed as the collision energy is varied. It was pointed out in Ref. [23] that such phase dislocation lines are topological invariants. That dislocation line extends along the negative  $x$  axis and is clearly visible in Fig. (2).

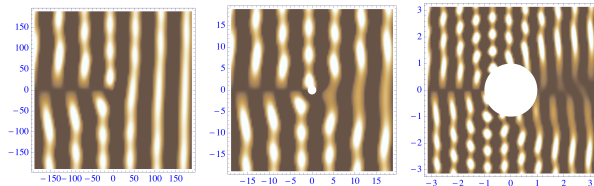


FIG. 2: Density plots of the imaginary part of  $\psi(R, \theta)$  as function of  $x$  (abscissa) and  $y$  (ordinate). The panels from left to right correspond to wave numbers  $k = 0.01, 1, 10$  respectively. The incident wave approaches from the right. The white disk at the center represents an impenetrable cylinder of radius  $a = 1$ .

In the calculations presented here we consider a molecular collision model that is expected to demonstrate Mead-Truhlar phase holonomy in the adiabatic (i.e. the BO) approximation. However we relax adiabaticity and, within the scope of this model, proceed to produce exact numerical solutions for the scattering problem. We use the resulting solutions to investigate whether the aforementioned, topological, AB-like phase discontinuities arise and persist as the collision energy is varied.

## B. Gauge potentials induced by conical intersections

Consider a tri-atomic system that possesses a conical intersection at the origin of a parameter space spanned by a set of nuclear internal coordinates  $x, y$ . Typically, they represent various linear combinations of the squares of inter-nuclear distances between the three nuclei[6] in a planar configuration. In this coordinate system the azimuthal angle  $\phi$  is called the pseudo-rotation and  $\rho = \sqrt{x^2 + y^2}$  measures distortions from an equilateral triangle configuration of nuclei. We describe the system by an amplitude  $\psi(x, y, \mathbf{r})$  where  $\mathbf{r}$  are electronic coordinates. Once the electronic, or fast, coordinates are integrated out the adiabatic Hamiltonian is a truncated two-dimensional Hilbert space operator, which in the vicinity of the intersection is given by[25]

$$H_{ad} = \begin{pmatrix} x & y \\ y & -x \end{pmatrix}. \quad (6)$$

The eigenvalues of  $H_{ad}$  are  $\pm\sqrt{x^2 + y^2}$  and correspond to first excited and ground states, respectively, of the electronic Hamiltonian. The eigenstates of  $H_{ad}(x, y)$  are parameterized by the nuclear coordinates and form the adiabatic basis for the PSS expansion, which for this model is complete. Figure (1) illustrates a typical conical intersection located at the origin of our coordinate system.

Because  $H_{ad}$  is real, Longuet-Higgins and Herzberg[26] constrained its eigenstates to be real-valued and found

$$\begin{aligned} |\Phi_g\rangle &= \begin{pmatrix} -\sin \phi/2 \\ \cos \phi/2 \end{pmatrix} = \tilde{U}(\phi)|g\rangle \\ \tilde{U}(\phi) &= \begin{pmatrix} \cos \phi/2 & -\sin \phi/2 \\ \sin \phi/2 & \cos \phi/2 \end{pmatrix} \\ |g\rangle &= \begin{pmatrix} 0 \\ 1 \end{pmatrix}, \quad |e\rangle = \begin{pmatrix} 1 \\ 0 \end{pmatrix}, \end{aligned} \quad (7)$$

where  $|\Phi_g\rangle$  is the ground adiabatic electronic state. They noted that it is multi-valued, as its value changes sign in traversing a circuit from  $\phi = 0$  to  $\phi = 2\pi$ . The total system amplitude  $\psi$  must be single valued and so in a Born-Oppenheimer approximation in which  $\psi = F(x, y)|\Phi_g\rangle$ , the vibronic amplitude  $F(x, y)$  must undergo a compensating sign change. That argument inspired Mead and Truhlar[6] to invoke the minimal coupling of the vibronic motion with the vector potential  $\mathbf{A}_{MAB}$ .

In this analysis we offer an alternative tack to that summarized above. Proceeding along the lines outlined in Ref. [21], which provides a general gauge theory setting for the PSS equations, we do not constrain the phases of the BO expansion basis  $\Phi_n(\mathbf{R}, \mathbf{r})$  but we do require them to be single valued for all  $\mathbf{R}$ . Applying this prescription to the model adiabatic Hamiltonian Eq. (6)

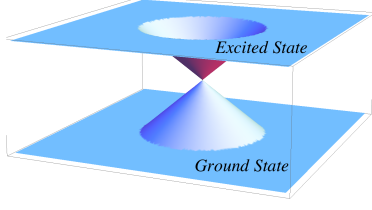


FIG. 3: (Color online). Illustration of a conical intersection between the ground BO surface and an excited electronic BO surface.

we find that

$$H_{ad} = U_c(\phi)H_{BO}U_c^\dagger(\phi)$$

$$H_{BO} = \begin{pmatrix} \sqrt{x^2 + y^2} & 0 \\ 0 & -\sqrt{x^2 + y^2} \end{pmatrix} \quad (8)$$

where

$$U_c(\phi) = \exp(-i\sigma_2\phi/2)\exp(i\sigma_3\phi/2) =$$

$$\begin{pmatrix} e^{i\frac{\phi}{2}} \cos\left(\frac{\phi}{2}\right) & -e^{-i\frac{\phi}{2}} \sin\left(\frac{\phi}{2}\right) \\ e^{i\frac{\phi}{2}} \sin\left(\frac{\phi}{2}\right) & e^{-i\frac{\phi}{2}} \cos\left(\frac{\phi}{2}\right) \end{pmatrix}. \quad (9)$$

Unlike the operator  $\tilde{U}(\phi)$  given in Eq. (7), which undergoes a sign change as  $\phi$  ranges from 0 to  $2\pi$ ,  $U_c(\phi)$  is single valued for all  $\phi$ , excluding the origin, i.e.  $U(\phi+2\pi) = U(\phi)$ . So we employ the **single-valued** eigenstates  $U_c(\phi)|g\rangle$ , and  $U_c(\phi)|e\rangle$  in our the PSS expansion. Taking the vibronic kinetic energy operator to have the form

$$H_{KE} = -\frac{\hbar^2}{2\mu} \left( \frac{\partial^2}{\partial x^2} + \frac{\partial^2}{\partial y^2} \right)$$

where  $\mu$  is a reduced atomic mass. We obtain (e.g see Ref.[24])

$$-\frac{\hbar^2}{2\mu} (\nabla - i\mathbf{A})^2 F(\mathbf{R}) + V(\mathbf{R})F(\mathbf{R}) = EF(\mathbf{R}). \quad (10)$$

$F(\mathbf{R})$  is a column vector whose two entries are the ground and excited state adiabatic vibronic amplitudes,  $V(\mathbf{R}) = H_{BO}(x, y)$  and  $\mathbf{A}$  is the matrix gauge potential

$$\mathbf{A} = iU_c^\dagger \nabla U_c = \frac{\hat{\phi}}{2\rho} \begin{pmatrix} -1 & -i \exp(-i\phi) \\ i \exp(i\phi) & 1 \end{pmatrix}. \quad (11)$$

Because the PSS expansion basis is complete, Eq. (10) is equivalent to the coupled equations obtained in the

adiabatic basis set i.e., the amplitude  $G(\mathbf{R}) = U_c(\phi)F(\mathbf{R})$  satisfies

$$-\frac{\hbar^2}{2\mu} \nabla^2 G(\mathbf{R}) + H_{ad}(x, y)G(\mathbf{R}) = EG(\mathbf{R}) \quad (12)$$

where  $H_{ad}(x, y)$  is given by Eq. (6).

In order to study collision phenomena, which require in-coming and out-going asymptotic packets, we introduce a slightly modified version of the LHH model, and in which the diabatic coupling is given by

$$H'_{ad}(x, y) = \Xi(\rho, \rho_0) \begin{pmatrix} x & y \\ y & -x \end{pmatrix}$$

$$\frac{\Xi}{\Delta} \equiv \frac{\theta(\rho - \rho_0)}{\rho} + \frac{\theta(\rho_0 - \rho)}{\rho_0} \quad (13)$$

where  $\rho_0, \Delta$  are constants and  $\theta$  is the Heaviside function. The eigenvalues of  $H'_{ad}(x, y)$  are

$$\begin{aligned} &\pm \Delta \quad \text{for } \rho > \rho_0 \\ &\pm \frac{\Delta}{\rho_0} \sqrt{x^2 + y^2} \quad \text{for } \rho \leq \rho_0. \end{aligned} \quad (14)$$

The BO eigenvalues of  $H'_{ad}(x, y)$  describe a conical intersection, centered on the origin but in the region  $\sqrt{x^2 + y^2} > \rho_0$  it consists of two flat surfaces separated by an energy gap  $2\Delta$ . The latter feature allows asymptotic incoming and outgoing scattering states. The BO surfaces, defined by Eq. (14), are illustrated in Figure (3). We now study the behavior of an asymptotic “free” wave packet as it approaches in the ground BO state and is scattered by the CI centered at the origin. To that end we employ the split operator method[27] to propagate the wave packet. At some initial time  $t_0$  we place a packet in the ground BO state shown in panel (a) of Figure (4). The mean velocity of the packet is chosen so that it approaches the origin at subsequent times  $t > t_0$ . Panels (b) and (c) of Figure (4) illustrate it’s time development as it approaches the CI, diffracts about it, and eventually continues, shown in panel (d), as a free, scattered, packet at the post collision time  $t_f$ . The detailed discussion of this calculation is summarized below.

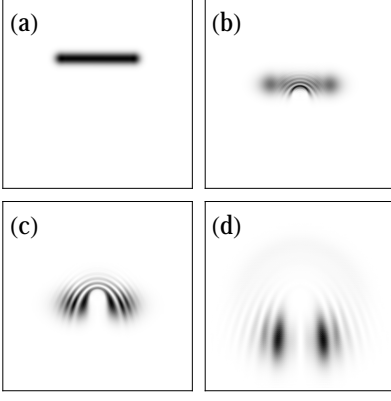


FIG. 4: Probability density plots of a vibronic packet being scattering by a conical intersection (not shown) in the ground BO state. Panel (a) shows initial wavepacket at  $t = t_0$ . Panels (b),(c) show packet incident on a CI that is located at the midpoint of each frame. Panel (d) illustrates scattered packet at  $t = t_f$ .

### C. Time dependent, multi-channel, propagation of wave packets in the diabatic picture

In the simulation outlined above, we make use of the split operator method[27] in order to propagate a packet that is, initially, asymptotically removed from the scattering center. We first define a set of dimensionless coordinates  $\xi = x/L, \eta = y/L$ , and time parameter  $\tau = \hbar t/2mL^2$  where  $L$  is an arbitrary length scale. The resulting time-dependent coupled equations for the diabatic amplitudes are

$$\begin{aligned} i\frac{\partial G_1}{\partial \tau} &= -\left(\frac{\partial^2 G_1}{\partial \xi^2} + \frac{\partial^2 G_1}{\partial \eta^2}\right) + \tilde{V}_{11}G_1 + \tilde{V}_{12}G_2 = 0 \\ i\frac{\partial G_2}{\partial \tau} &= -\left(\frac{\partial^2 G_2}{\partial \xi^2} + \frac{\partial^2 G_2}{\partial \eta^2}\right) + \tilde{V}_{21}G_1 + \tilde{V}_{22}G_2 = 0 \end{aligned} \quad (15)$$

where the rescaled couplings  $\tilde{V}_{ij}$  are given by

$$\begin{aligned} \tilde{V}_{11} &= -\tilde{V}_{22} = \Xi(\tilde{\rho}, \tilde{\rho}_0) \tilde{\Delta} \xi \\ \tilde{V}_{12} &= \tilde{V}_{21} = \Xi(\tilde{\rho}, \tilde{\rho}_0) \tilde{\Delta} \eta \end{aligned} \quad (16)$$

and

$$\begin{aligned} \tilde{\Delta} &= \frac{2mL^2\Delta}{\hbar^2} \\ \tilde{\rho} &= \sqrt{\xi^2 + \eta^2} \end{aligned} \quad (17)$$

are dimensionless parameters. We express the diabatic amplitudes in matrix form

$$G(\tau) \equiv \begin{pmatrix} G_1(\tau) \\ G_2(\tau) \end{pmatrix} \quad (18)$$

and apply the split-operator propagation algorithm[27]

$$G(\tau + \delta\tau) = U_{KE} U_V U_{KE} G(\tau) \quad (19)$$

where

$$U_{KE} = \exp\left(i\frac{\delta\tau}{2}\left(\frac{\partial^2}{\partial \xi^2} + \frac{\partial^2}{\partial \eta^2}\right)\right) \begin{pmatrix} 1 & 0 \\ 0 & 1 \end{pmatrix} \quad (20)$$

and

$$\begin{aligned} U_V &= \exp(-i\delta\tau H'_{ad}(x, y)) = \begin{pmatrix} U_{11} & U_{12} \\ U_{21} & U_{22} \end{pmatrix} \\ U_{11} &= \cos(\Delta(\xi, \eta)\delta\tau) - i\cos(\phi)\sin(\Delta(\xi, \eta)\delta\tau) \\ U_{12} &= U_{21} = -i\sin\phi\sin(\Delta(\xi, \eta)\delta\tau) \\ U_{22} &= \cos(\Delta(\xi, \eta)\delta\tau) + i\cos(\phi)\sin(\Delta(\xi, \eta)\delta\tau). \end{aligned} \quad (21)$$

Here  $2\Delta(\xi, \eta)$  is the energy defect between the two BO surfaces shown in Fig. (4),

$$\Delta(\xi, \eta) \equiv \Delta \quad \text{for } \tilde{\rho} > \tilde{\rho}_0; \quad \frac{\Delta}{\tilde{\rho}_0} \sqrt{\xi^2 + \eta^2} \quad \text{for } \tilde{\rho} \leq \tilde{\rho}_0 \quad (22)$$

where  $\phi$  is the pseudo-angle and  $\tan \phi = \eta/\xi$ .

With the repeated application of the propagation algorithm Eq. (19), the amplitude  $G(\tau)$  at  $\tau > \tau_0$  is obtained. The initial packet  $\psi_0(\tau_0)$  is chosen to be the finite slab shown in panel (a) of Figure (4). It is incident on the ground adiabatic branch and so we perform a transformation into the diabatic picture,

$$\begin{aligned} G(\tau_0) &= U_c^\dagger(\phi) F(\tau_0) \\ F(\tau_0) &= \begin{pmatrix} 0 \\ \psi_0(\tau_0) \end{pmatrix}. \end{aligned} \quad (23)$$

The parameters characterizing  $\psi_0$  are chosen so that the probability density is appreciable only in the asymptotic region where the ground BO surface has the flat landscape shown in that figure. It's initial velocity along the positive  $\xi$  direction allows it to proceed toward the origin. It encounters the conical intersection near the origin, shown by panels (b),(c) at interim values  $\tau_0 < \tau < \tau_f$ . At  $\tau_f$  the, scattered, packet continues into the, post collision, asymptotic ground BO landscape.

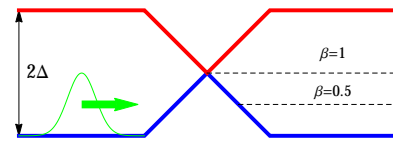


FIG. 5: (Color online). Schematic illustration of a packet impinging on a conical intersection for different values of  $\beta$ . The diagram (not drawn to scale) is a cross section intersecting the CI with an azimuthal symmetry plane. The blue line is the ground BO branch, whereas the red line represents the excited state branch.

Figure (5) illustrates the role of the ratio  $\beta \equiv k^2/\Delta$ , where  $k^2$  is the incident collision energy and  $\Delta$  the BO



energy defect parameter for the asymptotic region.  $\beta = 1$  is the value in which the collision energy is equal to the height of the ground branch of the conical intersection at the origin. For  $\beta = 1/2$  the packet energy is not sufficient to tunnel through the cone and so diffracts about it. The diffraction peaks are prominent in Figure (4). In this study we do not consider the case  $\beta \gg 1$ , for which non-adiabatic transitions into the excited state are allowed. Our calculations show that for  $\beta = 1$  a minute fraction  $< 1\%$  of the initial packet suffers a transition.

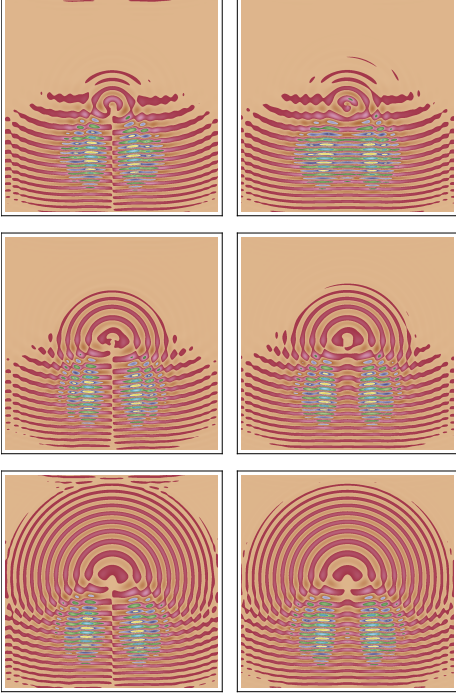


FIG. 6: (Color online). Density plots of the imaginary part of the packet amplitude at time  $t = t_f$ . Initial packet (not shown) at  $t_0$  is incident at the top of a frame and propagates toward the CI located at the mid-point of each panel. The row entries correspond to different values of ratio  $\beta = k^2/\Delta$ . Top row corresponds to  $\beta = 1$ , middle row to  $\beta = 1/2$ , and third row to  $\beta = 1/8$ . The left column illustrates solutions to Eq. (12) in which the adiabatic Hamiltonian is given by Eq. (13), whereas the right column plots the corresponding solutions for the latter defined in Eq. (27).

In Figure (6) we plot the imaginary part of the amplitude at the post collision time  $\tau_f$  in the  $\xi, \eta$  plane for the values of  $\beta = 1, 1/2, 1/8$ . The top row, and first column, of that figure illustrates the calculated amplitude for the value  $\beta = 1$ . The subsequent rows, in the first column, correspond to the cases  $\beta = 1/2$  and  $\beta = 1/8$  respectively. Those panels illustrate that as  $\beta$  decreases, back-scattering is enhanced. This behavior follows from the fact that smaller  $\beta$  imply classical turning points near the base and broader sections of the cone (see Fig. (5)).

Having developed the theory in the diabatic gauge, we

consider the coupled equations for the amplitudes  $F(\mathbf{R})$  in the adiabatic picture, or gauge. We express the adiabatic Hamiltonian, defined in Eq. (13), as

$$H'_{ad}(x, y) = U_c(\phi) H'_{BO} U_c^\dagger(\phi) \quad (24)$$

where  $H'_{BO}$  is the diagonal matrix whose eigenvalues are given by Eq. (14) and  $U_c$  is defined in Eq. (9). Proceeding with the PSS expansion, we arrive at Eq. (10), with the non-Abelian gauge potential  $\mathbf{A}$  given by Eq. (11), and the BO diagonal matrix now given by  $H'_{BO}$ . We perform a BO projection of it, onto the ground adiabatic state to get

$$-\frac{\hbar^2}{2\mu} (\nabla - i\mathbf{A}_P)^2 F_g(\mathbf{R}) + \tilde{V}_g(\mathbf{R}) F_g(\mathbf{R}) = E F_g(\mathbf{R}) \quad (25)$$

where

$$\mathbf{A}_P = Tr(P\mathbf{A}P) = \frac{\hat{\phi}}{2\rho} \quad (26)$$

is the projected component of the non-Abelian gauge potential  $\mathbf{A}$  and  $P$  is a projection operator.  $F_g(x, y)$  is the ground adiabatic amplitude and  $\tilde{V}_g(\mathbf{R})$  is the sum of the ground BO energy, given in Eq. (14), and the non-adiabatic scalar correction[21, 28, 29]  $\hbar^2/(2\mu\rho^2)$ . Because we chose collision energies smaller than the energy defect  $2\Delta$ , we expect that the projected BO equation (25) provides a good approximation to the amplitude obtained from solution of the fully coupled problem. In order to test this hypothesis we introduce a new adiabatic Hamiltonian

$$H''_{ad}(x, y) = \Xi(\rho, \rho_0) \begin{pmatrix} x & y \exp(-i\phi) \\ y \exp(i\phi) & -x \end{pmatrix} \quad (27)$$

which is a generalization[11] of  $H'_{ad}$  defined in Eq. (13).  $H''_{ad}$  shares identical potential surfaces to those predicted by  $H'_{ad}$  and given in Eq. (14). Indeed we find

$$H''_{ad}(x, y) = U_d H'_{BO} U_d^\dagger$$

$$U_d = \begin{pmatrix} e^{\frac{1}{2}i \sin(\phi) - \frac{i\phi}{2}} \cos\left(\frac{\phi}{2}\right) & -e^{-\frac{i\phi}{2} - \frac{1}{2}i \sin(\phi)} \sin\left(\frac{\phi}{2}\right) \\ e^{\frac{i\phi}{2} + \frac{1}{2}i \sin(\phi)} \sin\left(\frac{\phi}{2}\right) & e^{-\frac{1}{2}i \sin(\phi) + \frac{i\phi}{2}} \cos\left(\frac{\phi}{2}\right) \end{pmatrix}.$$

$H''_{ad}$  differs from  $H'_{ad}$  as it embeds  $H'_{BO}$  with unitary operator  $U_d$  instead of  $U_c$ . It is also evident that  $U_d$ , like  $U_c$ , is single-valued. With it we obtain the PSS equation (10) with  $V(\mathbf{R}) = H'_{BO}(x, y)$  and

$$\mathbf{A} = iU_d^\dagger \nabla U_d =$$

$$-\frac{\hat{\phi}}{2\rho} \begin{pmatrix} 0 & e^{-i \sin(\phi)} (\sin(\phi) + i) \\ e^{i \sin(\phi)} (\sin(\phi) - i) & 0 \end{pmatrix}.$$

Because the diagonal components of this matrix vanish, the BO projection of the PSS equations again leads to Eq. (25) but with the important difference that  $\mathbf{A}_P = 0$ . In

addition, the scalar non-adiabatic correction is modified to  $\hbar^2(1 + \sin^2(\phi))/(8\mu\rho^2)$ . According to the BO approximation, and the fact that  $\mathbf{A}_P = 0$ ,  $H''_{ad}$  does not allow a molecular AB effect despite the fact that  $H''_{ad}$  shares an identical CI to that predicted by  $H'_{ad}$ .

We propagate the packet in the diabatic picture, as described above, but replace  $H'_{ad}$  with  $H''_{ad}$ . The results of those simulations are shown in the second column of Fig. (6). In that figure, the rows correspond to results of calculations using the respective values for  $\beta$  itemized above. Note that the overall structure of the calculated amplitudes is similar to that shown by the panels in the first column. They both show similar trends in the backscattering amplitude as  $\beta$  varies, and validates the BO approximation in that the gross features of the elastic scattering amplitude are correctly predicted by the ground state BO potential  $V_{BO} = -\Delta/\rho_0 \sqrt{x^2 + y^2}$  in the region  $\rho < \rho_0$ . However, the amplitudes illustrated in the left column do not exactly match those on the right. The former amplitudes exhibit a prominent phase dislocation line that starts at the origin and proceeds along the positive  $x$  axis. This feature is absent in the corresponding panels of the second column in Figure (6) and appears to be independent of the collision parameter  $\beta$ . In appendix A it is shown how topological phase dislocation lines are a consequence of the induced Abelian vector potential  $\mathbf{A}_P$  that is explicit in the adiabatic gauge (representation).

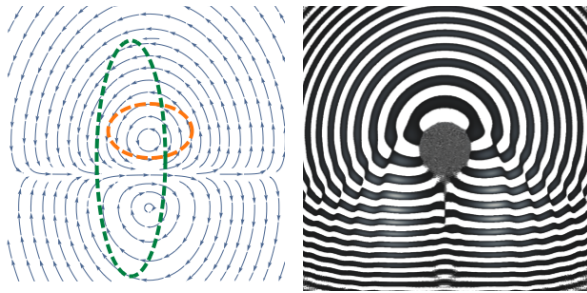


FIG. 7: (Color online). Left panel: Flow maps of the vector potential, that describe a pair of CI's, given in Eq. (30). Dashed lines represent closed paths that define Wilson loop integrals. Right panel: Complex component of vibronic amplitude, as it is scattered by the pair of CI's located at the origin, and a point downwind from the scattering center. The dark circular shaded region centered at the origin represents an impenetrable obstacle. The phase dislocation line terminating at the point  $\xi = 0, \eta_0 = 3$  is clearly visible in the figure.

## II. SUMMARY AND CONCLUSION

We introduced a two-state molecular collision model which features a conical intersection that asymptotically

correlates to a pair of BO states separated by a finite energy gap  $2\Delta$ . For it, we numerically solved the time dependent Schroedinger equation in the diabatic gauge (representation). An incident wavepacket of mean energy, less than the energy gap, was chosen and propagated in time as it was scattered by the conical intersection. The global phase structure of the vibronic amplitudes was analyzed and found to exhibit an underlying topological order associated with phase dislocation lines identical to ones observed in standard AB scattering. The dislocation lines, suggesting fractional topological charge, are not affected by variation in the total collision energy as long the inequality  $k^2/2\mu < 2\Delta$  is satisfied. We conclude that this feature demonstrates persistence of topological behavior beyond the strictly adiabatic limit. It differs from the conclusions of a previous study[20] that argues survival of the MAB effect only in the limit where  $\mu \rightarrow \infty$ . The results of our numerical study, that does not rely on the BO approximation, confirms the fidelity of the latter in applications for realistic molecular collision systems provided that a gauge vector potential is minimally coupled to the vibronic amplitude in the adiabatic gauge.

There have been numerous efforts over the decades to predict observable MAB behavior in reactive scattering settings, but, as of yet, there exist no compelling evidence of the latter in reports of laboratory measurements. One explanation that is offered for the lack of a MAB “smoking gun” is the possibility of cancellation of partial-wave phase shifts generated by the CI scalar potential with that produced by the Mead-Truhlar vector potential. A recent study[30] argued that this cancellation effect might be circumvented in ultra-cold molecular collisions where s-wave scattering dominates. According to Wigner threshold theory, phase shifts generated by a short range potential scale as a power of the incident collision wave number and therefore the partial wave phase shifts  $\delta(k) \rightarrow 0$  as  $k \rightarrow 0$ . In the ultra-cold limit the leading order contribution to the cross section is generated by the isotropic s-wave. However, the presence of a long range vector potential  $\mathbf{A}_{MAB}$  predicts phase shifts  $|\delta_{MAB}|_m = \pi/2$  for the  $m$ 'th partial wave [31, 32]. In pure AB scattering, the leading order term that survives in the  $kR \rightarrow 0$  limit is (see Appendix A) proportional to

$$J_{1/2}(kR)(1 + \exp(i\phi)) \quad (28)$$

and differs from standard 2D s-wave behavior by the fact that the radial term  $J_{1/2}$  vanishes at the origin, and both the  $s$  and  $p$ -waves contribute identical phase shifts. Also, in contrast to short range potentials in which only s-waves survive in the ultra-cold limit, Eq. (28) predicts anisotropic scattering. Here we propose an additional mechanism by which AB phase shifts at larger impact parameters may be suppressed. If  $\mathbf{A}_{MAB}$  is screened at larger internuclear distances due to multiple CI's, does the MAB effect arise in the ultra-cold limit? In order to address this question, within the scope of our 2-state model, we need to calculate the gauge structure of a gen-

eral electronic (2-state) model Hamiltonian

$$H_{ad}(x, y) = \begin{pmatrix} h(x, y) & g(x, y) \\ g(x, y) & -h(x, y) \end{pmatrix}. \quad (29)$$

The regular, real-valued, functions  $h(x, y), g(x, y)$  were chosen (see appendix B) so that  $H_{ad}$  possesses a pair of conical intersections located at the origin and at a point downwind ( $x = x_0, y = 0$ ) from the scattering center. In addition to the conical intersection potential surface, we added a radial symmetric barrier centered at the origin in order to define a scattering center. In right the hand panel of Fig. (7) we plot the imaginary part of the vibronic amplitude in order to uncover its global phase structure. Clearly evident in this figure is a phase dislocation line, starting at the origin (not show because tunneling into the radial barrier is prevented) and extending along the vertical scattering axis. However, unlike the case discussed in the previous sections, the phase dislocation line terminates at the location of the second conical intersection. According to the results of Appendix B the gauge potentials associated with this pair of CI's is

$$\begin{aligned} A_x &= \frac{y(2x - x_0)}{2(y^2 + x^2(x_0 - x)^2)} \\ A_y &= \frac{x(x_0 - x)}{2(y^2 + x^2(x_0 - x)^2)}. \end{aligned} \quad (30)$$

In the left-most panel of Fig. (7) we plot streamlines for vector potential  $\mathbf{A}$  whose components are given by Eq. (30). Superimposed, in this figure, are closed paths  $C_i$  for which we evaluate the Abelian Wilson loop integral for  $\mathbf{A}$  i.e.

$$\exp(i \oint_{C_i} \mathbf{A} \cdot d\mathbf{R}).$$

For the loop that encloses only a single CI, shown by the orange line in that figure, the integral has the value  $-1$ , in contrast to value obtained,  $+1$ , for the (green) loop that encloses both CI's. In the latter, topological holonomy is absent. Our observation is in harmony with the conclusion of previous investigations of systems possessing a CI pair [33]. How this effective screening at larger impact parameters affects scattering properties, at both the ultra-cold and high energy limits is under current investigation. In addition, we pose the question: what happens when the collision energy is much larger than the energy defect  $\Delta$  between the ground and excited electronic BO surfaces. Evidence gleaned from recent investigations concerning geometric phase effects in two-state systems[24, 34], as well as in spinor Bose-Fermi mixtures[35], suggests a transition from Abelian to non-Abelian behavior and in the limit where  $k^2/2\mu \gg \Delta$  decoupling to a null effect. If and how this Abelian to non-Abelian crossover occurs in molecular systems is an open question and deserves closer examination.

## ACKNOWLEDGMENTS

I wish to acknowledge support by the NSCEE for use of the Intel Cherry-Creek computing cluster.

### Appendix A: Topological charge of $\Psi_{AB}$

Consider a complex scalar field in two dimensions and express it in the form  $\psi(x, y) = \rho(x, y) \exp(i\chi(x, y))$  where  $\rho(x, y) \geq 0$  and  $\chi$  are real functions. The quantity

$$S_C \equiv \frac{1}{2\pi} \oint_C d\mathbf{R} \cdot \nabla \chi, \quad (A1)$$

where  $C$  is a closed loop (not crossing the zeros of  $\rho$ ) is called the topological charge[23, 36]. Below we offer an illustration of this property in solutions of the Schroedinger equation that is minimally coupled to the vector potential  $\mathbf{A}_{MAB}$ .

Consider the partial wave solutions of the AB equation[1]

$$J_{|m-\alpha|}(kr) \exp(im\phi) \quad (A2)$$

where  $m$  is an integer. They possess nodal lines at the zeros of  $J_{|m-\alpha|}$  and in the annular region between two nodes,  $\chi = m\phi + \phi_0$  where the constant  $\phi_0 = 0, \pi$  corresponds to the cases where  $J_{|m-\alpha|}$  is positive and negative respectively. Thus  $S_C$  in a given region (not crossing the nodal lines) has integer topological charge  $m$ . For  $\alpha = 1/2$  we construct the linear combination of the  $m = 0, 1$  partial waves

$$\begin{aligned} \tilde{\psi}(r, \phi) &\equiv J_{|0-1/2|}(kr) + J_{|1-1/2|}(kr) \exp(i\phi) = \\ &J_{1/2}(kr) \left( 1 + \exp(i\phi) \right), \end{aligned} \quad (A3)$$

which is proportional to the leading order term in the  $kr \rightarrow 0$  limit of  $\psi_{AB}$ . In addition to the concentric nodal line structure described above,  $\tilde{\psi}$  vanishes along the negative  $x$  axis ( $\phi = \pi$ ) and we find  $\chi = \phi/2 \pm \phi_0$  in a given annular region. Because  $\chi$  is not defined on a nodal line, we allow loops  $C$  in a given annular region that start at  $\phi = -\pi$  and end at  $\phi = \pi$ . Now, using Eq. (A3),

$$\nabla \chi = Im \left( \frac{\tilde{\psi}^\dagger \nabla \tilde{\psi}}{\tilde{\psi}^\dagger \tilde{\psi}} \right) = \frac{\hat{\phi}}{r} Im \left( \frac{\exp(i\phi)}{(\exp(i\phi) + 1)} \right)$$

and so the topological charge

$$S_C = \frac{1}{2\pi} \int_{-\pi}^{\pi} d\phi \frac{1}{2}$$

has the fractional value  $1/2$ . It is topological in the sense that the phase discontinuity along the negative  $x$ -axis persists regardless of the wavenumber  $k$ , and, as we demonstrate below, the nature of the short range potential.



In the scattering region, the most general solution can be expressed as a partial wave expansion

$$\psi(r, \phi) = \sum_{m=-\infty}^{\infty} \exp(im\phi) \times (a_m J_{|\alpha-m|}(kr) + b_m H_{|\alpha-m|}^{(1)}(kr)) \quad (\text{A4})$$

where the coefficients  $a_m, b_m$  are uniquely determined by the asymptotic boundary conditions and the requirement that Eq. (A4) match the logarithmic derivatives of the  $m$ 'th radial partial wave at some matching distance  $r_c$ . The radial wavefunctions  $R_m(r)$  obey

$$R_m''(r) + \frac{R_m'(r)}{r} - \frac{(m-\alpha)^2}{r^2} R_m(r) + (k^2 - U(r)) R_m(r) = 0 \quad (\text{A5})$$

and for  $\alpha = 1/2$  we find that  $R_m$  is identical for values where  $|m - 1/2| = (2n + 1)/2$  and  $n = 0, 1, 2, \dots$ . We construct the logarithmic derivative

$$y_m \equiv k R_m'(kr_c) / R_m(kr_c) \quad (\text{A6})$$

at the matching distance.  $y_m$ , is also invariant for  $m$  that satisfy  $|m - 1/2| = (2n + 1)/2$ . As we require the incoming wave to have the form  $\exp(-ikr \cos(\phi)) \exp(i\phi/2)$  [1] we find that

$$a_m = (-i)^{|m-\alpha|} \quad b_m = (-i)^{|m-\alpha|} \frac{y_m J_{|m-\alpha|} - J'_{|m-\alpha|}}{H'_{|m-\alpha|}^{(1)} - y_m H_{|m-\alpha|}^{(1)}}. \quad (\text{A7})$$

On the r.h.s of this equation the Bessel functions, and their derivatives, are evaluated at  $kr_c$ . For  $\alpha = 1/2$  we note that

$$a_{-n} = a_{n+1} \quad b_{-n} = b_{n+1} \quad (\text{A8})$$

where  $n = 0, 1, 2, \dots$ . Using this relation we can re-write Eq. (A4) in the form

$$\sum_{n=1}^{\infty} \exp(in\phi) \Phi_n(\phi) \times [a_n J_{n-1/2}(kr) + b_n H_{n-1/2}^{(1)}(kr)] \quad \Phi_n(\phi) \equiv 1 + \exp(-i(2n+1)\phi). \quad (\text{A9})$$

Because  $\Phi_n(\pm\pi)$  vanishes identically and is an odd function of  $\phi$  about  $\phi = \pm\pi$  for all  $n$ ,  $\psi(r, \phi)$  suffers a phase discontinuity along this line. The phase dislocation shows prominently in the illustrations in Fig (2). It is independent of both the collision energy (or wavenumber  $k$ ) and the parameters that define the short range potential.

## Appendix B: Multiple conical intersections

Consider the Hamiltonian

$$H(x, y) = \begin{pmatrix} h(x, y) & g(x, y) \\ g(x, y) & -h(x, y) \end{pmatrix} \quad (\text{B1})$$

where  $h(x, y) \equiv h, g(x, y) \equiv g$  are continuous real-valued functions defined on the 2D  $x, y$  plane. We consider only those functions in which  $H(x, y)$  possess a finite set of discrete zeros. The eigenvalues of  $H$  are  $E = \pm\sqrt{g^2 + h^2}$ . The square root symbol refers to the positive branch. Expressing the eigenvectors in matrix form

$$\psi \equiv \begin{pmatrix} c_1 \\ c_2 \end{pmatrix} \quad (\text{B2})$$

we require, for the lower energy eigenvalue  $E_- = -\sqrt{g^2 + h^2}$

$$c_1(h + \sqrt{g^2 + h^2}) + c_2 g = 0 \quad (\text{B3})$$

and find a possible (unnormalized) real eigenvector for  $E_-$

$$\tilde{\psi}_a = \begin{pmatrix} h - \sqrt{g^2 + h^2} \\ g \end{pmatrix} \quad (\text{B4})$$

Because  $h, g$  are regular on the  $x, y$  plane so is  $\tilde{\psi}_a$ , however if there are lines  $\mathcal{C}$  in the  $x, y$  plane in which  $g(x, y) = 0$  then  $\tilde{\psi}_a$  cannot be normalized in the regions where  $h(x, y) \geq |h(x, y)| \cap \mathcal{C}$ .

We therefore define a new (real-valued) eigenvector

$$\tilde{\psi}_b = \begin{pmatrix} g \\ -h - \sqrt{g^2 + h^2} \end{pmatrix} \quad (\text{B5})$$

which does not vanish in the region where  $\tilde{\psi}_a = 0$ .  $\tilde{\psi}_a, \tilde{\psi}_b$  are not linearly independent in the regions where they both have positive norm. However we can define the complex-valued eigenstate

$$\begin{aligned} \psi_- &\equiv \psi_a(x, y) + i \psi_b(x, y) \\ \psi_a &\equiv \frac{\tilde{\psi}_a}{2\sqrt{g^2 + h^2}} \\ \psi_b &\equiv \frac{\tilde{\psi}_b}{2\sqrt{g^2 + h^2}}. \end{aligned}$$

$\psi_-$  is normalized to unity and, with the exception of isolated points  $P_i = (x_i, y_i)$  in which  $h(P_i)$  and  $g(P_i)$  vanish identically, it is well behaved everywhere.

In the same manner we obtain the normalized complex-valued eigenvector  $\psi_+$  for the branch  $E_+ = \sqrt{g^2 + h^2}$ .

$$\begin{aligned} \psi_+ &\equiv \psi_c(x, y) + i \psi_d(x, y) \\ \psi_c &\equiv \frac{\tilde{\psi}_c}{2\sqrt{g^2 + h^2}} \quad \psi_d \equiv \frac{\tilde{\psi}_d}{2\sqrt{g^2 + h^2}}. \\ \tilde{\psi}_c &= \begin{pmatrix} h + \sqrt{g^2 + h^2} \\ g \end{pmatrix} \\ \tilde{\psi}_d &= \begin{pmatrix} g \\ -h + \sqrt{g^2 + h^2} \end{pmatrix} \end{aligned} \quad (\text{B6})$$

From these solutions we can construct the unitary matrix

$$U \equiv \frac{1}{2\sqrt{g^2 + h^2}} \begin{pmatrix} h + \sqrt{g^2 + h^2} + ig & -g - i(h - \sqrt{g^2 + h^2}) \\ g + i(-h + \sqrt{g^2 + h^2}) & -ig + h + \sqrt{g^2 + h^2} \end{pmatrix} \quad (\text{B7})$$

It is single-valued everywhere except at the points  $P_i$  defined above.  $U$  diagonalizes Hamiltonian Eq.(B1) so that

$$H = U^\dagger H_{BO} U$$

where

$$H_{BO} \equiv \begin{pmatrix} \sqrt{h^2 + g^2} & 0 \\ 0 & -\sqrt{h^2 + g^2} \end{pmatrix}. \quad (\text{B8})$$

For the special case  $h(x, y) = x, g(x, y) = y$  we obtain the unitary operator defined in Eq. (9). From  $U$  we obtain the non-Abelian gauge potential

$$\mathbf{A} \equiv iU^\dagger \nabla U. \quad (\text{B9})$$

It is a pure gauge[24, 37] in the sense that the Wilson loop integral satisfies the identity

$$P \exp(i \int_C \mathbf{A} \cdot d\mathbf{R}) = \mathbf{I}, \quad (\text{B10})$$

where  $C$  is any closed loop that does not intersect  $P_i$  in the  $x, y$  plane,  $\mathbf{I}$  the unit matrix, and  $P$  refers to a path-ordered integral[24]. However the projected gauge potential

$$\mathbf{A}_g \equiv \text{Tr } P_g \mathbf{A} P_g \quad (\text{B11})$$

may be non-trivial and necessarily not satisfy Eq. (B10). Here  $P_g$  is a projection operator into the ground state of  $H_{BO}$ .

Using definitions Eqs. (B7), (B9) and Eq. (B11) we find

$$\mathbf{A}_g = \frac{h \nabla g - g \nabla h}{2(g^2 + h^2)}. \quad (\text{B12})$$

Evaluating the curvature  $\mathbf{H} = \nabla \times \mathbf{A}_g$  we find that it vanishes identically except possibly at the points  $P_i$  where  $\mathbf{A}_g$  is singular. Suppose a set  $n$  of such points  $P_1, P_2 \dots P_n$  exist. We now construct a line integral

$$\int_C d\mathbf{r} \cdot \mathbf{A}_g \quad (\text{B13})$$

where  $C$  is a circular contour of radius  $R$  centered at the origin. According to Stokes theorem, and the fact that  $\mathbf{H} = 0$  in the region not including these points, we find

$$\int_C d\mathbf{r} \cdot \mathbf{A}_g = \sum_i^n \int_{C_i} d\mathbf{r} \cdot \mathbf{A}_g \quad (\text{B14})$$

where  $C_i$  is the infinitesimal contour surrounding the point  $P_i$ . If integration along  $C$  is counterclockwise so it is with the paths  $C_i$ .

Let us consider the line integral surrounding the point  $P_0 = (x_0, y_0)$ . We define the coordinates  $x' = \rho \cos \phi, y' = \rho \sin \phi$  where  $\rho$  is the distance from a point  $x, y$  on the path  $C_0$  to  $P_0$  and  $\phi$  is the angle of a line from  $P_0$  to a point on  $C_0$  makes with the  $x'$  axis. We then get

$$\int_{C_0} d\mathbf{r} \cdot \mathbf{A}_g = \int_0^{2\pi} d\phi \left( \frac{h \partial_\phi g - g \partial_\phi h}{2(g^2 + h^2)} \right). \quad (\text{B15})$$

Because we can shrink  $C_0$  arbitrarily close to  $P_0$  we can express  $h, g$  in that neighborhood as

$$\begin{aligned} h(x', y') &\approx h_x \rho \cos \phi + h_y \rho \sin \phi \\ g(x', y') &\approx g_x \rho \cos \phi + g_y \rho \sin \phi \end{aligned} \quad (\text{B16})$$

where the constant

$$h_x \equiv \frac{\partial h}{\partial x}$$

is evaluated at the point  $P_0$  and we used the fact that  $h(P_0) = g(P_0) = 0$ . The constants  $h_y, g_x, g_y$  are defined in a similar way. Inserting expressions Eq. (B16) into Eq. (B15), we obtain

$$\int_{C_0} d\mathbf{r} \cdot \mathbf{A}_g = \int_0^{2\pi} d\phi \frac{g_y h_x - h_y g_x}{2((g_x^2 + h_x^2) \cos^2 \phi + (g_y^2 + h_y^2) \sin^2 \phi + (g_x g_y + h_x h_y) \sin 2\phi)}. \quad (\text{B17})$$

The second integral is evaluated to give,

$$\int_{C_0} d\mathbf{r} \cdot \mathbf{A}_g = \text{sgn}(g_y h_x - h_y g_x) \pi. \quad (\text{B18})$$

Using this result and Eq. (B14) we make the following observation for the Abelian Wilson loop integral,

$$\exp(i \int_C d\mathbf{r} \cdot \mathbf{A}_g) = \pm 1 \quad (\text{B19})$$

for the cases where  $C$  encloses an even number, or odd,

number of singularities respectively (provided that the r.h.s. of Eq. (B18) does not vanish).

- 
- [1] A. Aharonov and D. Bohm, Phys. Rev. **115**, 485 (1959).
  - [2] W. Ehrenberg and R. E. Siday, Proceedings of the Physical Society. Section B **62**, 8 (1949).
  - [3] F. Wilczek, Physical Review Letters **49**, 957 (1982).
  - [4] R. B. Laughlin, Phys. Rev. Lett. **50**, 1395 (1983).
  - [5] M. Z. Hasan and C. L. Kane, Rev. Mod. Phys. **82**, 3045 (2010).
  - [6] C. A. Mead and G. D. Truhlar, The Journal of Chemical Physics **70**, 2284 (1979).
  - [7] M. Peshkin, Physics Reports **80**, 375 (1981).
  - [8] C. A. Mead, Chemical Physics **49**, 23 (1980).
  - [9] G. Delacrétaz, E. R. Grant, R. L. Whetten, L. Wöste, and J. W. Zwanziger, Phys. Rev. Lett. **56**, 2598 (1986).
  - [10] H. von Busch, V. Dev, H.-A. Eckel, S. Kasahara, J. Wang, W. Demtröder, P. Sebal, and W. Meyer, Phys. Rev. Lett. **81**, 4584 (1998).
  - [11] J. W. Zwanziger and E. R. Grant, J. Chem. Phys. **87**, 2950 (1987).
  - [12] Y.-S. M. Wu and A. Kuppermann, Chem. Phys. Lett. **201**, 178 (1993).
  - [13] B. G. Levi, Physics Today **46**, 17 (1993).
  - [14] D. E. Adelman, N. E. Shafer, D. A. V. Kliner, and R. N. Zare, J. Chem. Phys. **97**, 7323 (1992).
  - [15] E. Wrede, L. Schnieder, K. Welge, F. Aoiz, L. Bañares, and V. Herrero, Chemical Physics Letters **265**, 129 (1997).
  - [16] B. K. Kendrick, J. Chem. Phys. **112**, 5679 (2000).
  - [17] J. C. Juanes-Marcos and S. C. Althorpe, The Journal of Chemical Physics **122**, 204324 (2005).
  - [18] J. C. Juanes-Marcos, S. C. Althorpe, and E. Wrede, Science **309**, 1227 (2005).
  - [19] J. Jankunas, M. Sneha, R. N. Zare, F. Bouakline, S. C. Althorpe, D. Herráez-Aguilar, and F. J. Aoiz, Proceedings of the National Academy of Sciences **111**, 15 (2014).
  - [20] S. K. Min, A. Abedi, K. S. Kim, and E. K. U. Gross, Phys. Rev. Lett. (2015).
  - [21] B. Zygelman, Phys. Lett. A **125**, 476 (1987).
  - [22] J. Moody, A. Shapere, and F. Wilczek, Phys. Rev. Lett. **56**, 893 (1986).
  - [23] M. V. Berry, R. G. Chambers, M. D. Large, C. Upstill, and J. C. Walmsey, Eur. J. Phys. **1**, 154 (1980).
  - [24] B. Zygelman, Physical Review A **92**, 043620 (2015).
  - [25] E. Teller, The Journal of Physical Chemistry **41**, 109 (1937).
  - [26] G. Herzberg and H. C. Longuet-Higgins, Discuss. Faraday Soc. **35**, 77 (1963).
  - [27] M. R. Hermann and J. A. Fleck, Phys. Rev. A **38** (1988).
  - [28] B. Zygelman and A. Dalgarno, Phys. Rev. A. **33**, 3853 (1986).
  - [29] B. Zygelman, Physical Review Letters **64**, 256 (1990).
  - [30] B. K. Kendrick, J. Hazra, and N. Balakrishnan, Phys Rev Lett **115**, 153201 (2015).
  - [31] Y. Aharonov, C. K. Au, E. C. Lerner, and J. Q. Liang, Phys. Rev. D **29**, 2396 (1984).
  - [32] W. C. Henneberger, Phys. Rev. A. **22**, 1383 (1980).
  - [33] D. R. Yarkony, Journal of Chemical Physics **110**, 701 (1999).
  - [34] B. Zygelman, Phys. Rev. A. **86**, 042704 (2012).
  - [35] N. T. Phuc, G. Tatara, Y. Kawaguchi, and M. Ueda, Nature Commun. **6**, 9135 (2015).
  - [36] M. Dennis, *Topological Singularities in Wave Fields*, Ph.D. thesis, University of Bristol (2001).
  - [37] In some literature, the term pure gauge is applied to vector potentials (connections) whose curvature vanishes but which may possess, as does the AB vector potential, a non-trivial Wilson loop phase. Here, we reserve this terminology for connections that have vanishing curvature and whose Wilson phase loop integral is unity. With the latter definition, one can always find a non-singular gauge transformation in which  $\mathbf{A} = 0$ .